5 Synthesis and characterization of Gd^{3+} doped system $SrCe_{1-x}Gd_xO_3$ (x=0.0,0.02,0.04,0.06 and 0.10)

5.1 Introduction

Proton conducting electrolyte materials are of great interest because of their wide applications. Specific applications of these electrolyte materials are in fuel cell, gas sensors, hydrogen separation membrane or high temperature electrolyte [237, 238, 74, 239]. Proton conducting electrolytes immerged as an alternative for well-known oxygen ions conducting electrolytes for Solid Oxide Fuel Cells (SOFC). Conversion of hydrogen using a solid oxide fuel cell (SOFC) with a proton-conducting electrolyte (protonic ceramic fuel cell, PCFC) occurs at an intermediate temperature (400-800 °C) without expensive electrocatalysts or necessity to recirculate the fuel [129]. Additional advantages, generally associated with oxide-ion-based SOFCs, include modularity of structure and cogeneration of heat and electricity. The use of HTPC materials as hydrogen and humidity sensors, [240-243] chemical reactors for ammonia generation, 12 partial oxidation13 and reforming14 of methane, and electrochemical promotion of oxidation15 has also been investigated.

Iwahara et.al. discovered in 1993 discovered well known perovskite oxides (Sr ,Ba)(Ce, Zr)$O_{3-\delta}$ high temperature proton conductors (HTPC) [129]. Since then numerous studies (experimental as well as computational) have been made to explore proton conduction in other perovskite oxides [242,243]. $ACeO_3$ (where A=Ba, Sr) are important members of perovskite family used for intermediate and high temperature applications such as fuel cells and electrocatalysis. In $ACeO_3$, Ce^{4+} has been partially replaced by trivalent metal ions such as Y^{3+}, Yb^{3+}, Gd^{3+}, Sm^{3+}, Nd^{3+}, giving compositions, $ACe_{1-x}M_xO_{3-x/2}$ [17, 129, 240-242]. On substitution of these trivalent ions at tetravalent ion (Ce^{4+}) sites, charge imbalance is compensated by generation of oxygen vacancies ($V_o^{\cdot\cdot}$). The oxygen deficient $ACe_{1-x}M_xO_{3-x/2}$ compounds reactive with H_2O molecules if they exposed to humid atmosphere. Using Kroger-Vink notations, this hydration reaction is written according to **Eq (5.1)**

$$H_2O(g) + V_O^{\cdot\cdot} + O_O^x \overset{yield}{\longleftrightarrow} 2OH_O^{\cdot} \quad (5.1)$$

Thus, presence of oxygen vacancies is absolutely necessary for water incorporation into the lattice [244]. From the literature survey, it has been found that doping of gadolinium at Ce^{4+} sites of $BaCeO_3$ improved proton conducting properties. Several investigations have been made on Gd doped $BaCeO_3$ solid solution, $BaCe_{1-x}Gd_xO_3$ [245, 246, 206]. On the contrary, limited investigations have been carried out on Gd doped $SrCeO_3$ solid solution $SrCe_{1-x}Gd_xO_3$ [247]. A systematic study to know the effect of Gd doping at Ce site of $SrCeO_3$ is missing in the literature. Hence in this work, an attempt has been made to incorporate Gd at Ce site and study the effect of Gd concentration on the structure and electrical properties of $SrCeO_3$. The difference in the ionic radius of Ce^{4+} and Gd^{3+} (in 6-cordination number) is only 8 % , hence higher solubility limit of Gd in the lattice of $SrCeO_3$ is expected. In this work, selected compositions of $SrCe_{1-x}Gd_xO_{3-\delta}$ (x = 0.00, 0.02, 0.04, 0.06 and 0.10) have been synthesized by convention solid state reaction method. Synthesized powders have been characterized using TGA-DSC, XRD, Raman spectroscopy, FTIR, UV- Visible techniques. AC electrical measurements of sintered pellets have been carried out in the temperature range 300-600 ^oC and frequency range 10 Hz – 20 MHz.

5.2 Experimental

The system $SrCe_{1-x}Gd_xO_{3-\delta}$ with x = 0.00, 0.02, 0.04, 0.06 and 0.10, abbreviated respectively as SCG0, SCG2, SCG4, SCG6 and SCG10 have been synthesized by solid state reaction method. $SrCO_3$ (Purity 99.9%, Alfa Aesar), cerium oxide CeO_2, and Gd_2O_3 (Purity 99.5%, Alfa Aesar) were taken as raw materials. Raw material CeO_2 was obtained from the heat treatment of ammonium nitrate $(NH_4)_2Ce(NO_3)_6$ (Purity 99.5%, Alfa Aesar) at 500 °C. A detailed synthesis and characterization procedure have already been discussed in chapter 2.

Simultaneous differential thermal analysis (DTA) and thermo gravimetric analysis (TGA) of the ash prepared powder was carried out using thermal analyser (Mettler Toledo, Germany), in the temperature range of 30–1000 °C with a heating rate of 10 °C/min in a nitrogen atmosphere. Powder X-ray diffraction (XRD) pattern was recorded using Rigaku Miniflex II Desktop X-ray Diffractometer. To understand the chemical state XPS spectra of a few compositions was studied. The Raman spectra of the samples were recorded in the wave number range 50 - 800 cm^{-1} using Raman spectrometer (T64000, Jovin-Yvon Horiba, France). Fourier transform of infrared (FTIR) spectra of the calcined powders were recorded in wave number range 400 - 4000 cm^{-1} by the spectroscope (Shimadzu, Model DF 803, Japan) using KBr pellet method. The UV – Visible spectra of the calcined powders have been collected in the wavelength range of 150 - 1000 nm in absorption mode by a spectrometer (V-770, Jasco, Japan). The microstructure and chemical composition of the fractured surfaces of the sintered pellets were examined using Scanning Electron Microscope (EVO18, Zeiss, Japan). Electrical measurements were performed on the silver coated pellet using two probe methods in the frequency range 20 Hz to 2 MHz using with 1 V applied a c signal using a LCR meter (Agilent - 4980 A, USA) in the temperature range 300–600 °C in the air.

5.3 Results and Discussion

5.3.1 Phase analysis and structural characterization using XRD

The room temperature x-ray diffraction pattern of the calcined powder of the samples is shown in **Figure 5.1**. The recorded XRD pattern of the samples was matched with JCPDS file (card no. 89-5546) available in the literature for the orthorhombic $SrCeO_3$. Positions and intensity of various peaks according to JCPDS file is included for reference in **Figure 5.1**. All the peaks observed in the XRD pattern of the samples matched with peaks reported in the JCPDS file. No additional peaks corresponding to raw materials $SrCeO_3$, CeO_2, Gd_2O_3 and commonly found secondary phase Sr_2CeO_4 were not seen in the pattern of the samples, which confirmed the formation of single-phase solid solution for all the compositions.

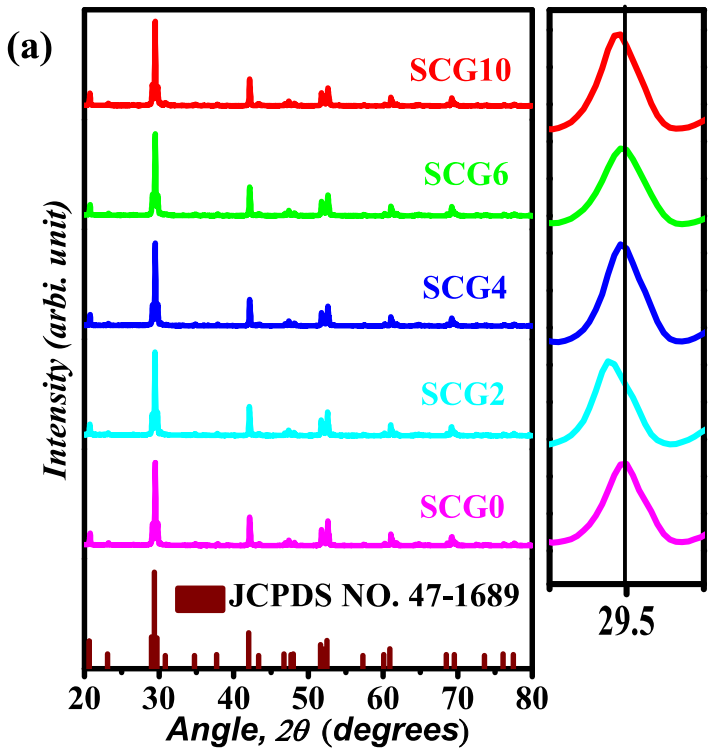

Figure 5.1 (a) Room temperature powder X-ray diffraction (XRD) and **(b)** magnified view of (112) peak of the samples.

In the literature, reports are available on substitution of Gd at both A and B sites of ABO_3 perovskite oxides[238] To check the site occupancy of dopant (Gd^{3+}) in the synthesized solid solution $SrCe_{1-x}Gd_xO_{3-\delta}$, the highest intensity peak corresponding to (130) reflection is plotted on expanded scale and shown in **Figure 5.1 (b)**. The position of peak of doped samples was compared with undoped sample (SCG0). Except for the composition with x=0.02, position of the peak for the doped samples (with x = 0.04, 0.06 and 0.10) is same as for the undoped sample (x=0.00, SCG0). A small shift ($\Delta 2\theta = 0.04°$) toward left or small angle side in the position of peak for the samples x=0.02 (SCG2) is seen in the XRD pattern. In the unit cell of perovskite oxide $SrCeO_3$, coordination number of Sr ions is twelve and of Ce ions is six. The ionic radius of Sr^{2+} and Gd^{3+} in 12-fold co-ordination is 1.44 Å, 1.27 Å, respectively. On the other hand, the ionic radius of Ce^{4+} and Gd^{4+} in 6-fold co-ordination is 0.87 Å and 0.938 Å, respectively. In 12-fold coordination the ionic radius of Gd^{3+} is 13.19 % smaller than Sr^{2+}. However, in 6-fold coordination the ionic radius of Gd^{3+} is 7.8 % larger Ce^{4+}. The size-mismatches between Sr and Gd; Ce and Gd is within the limit mentioned by the Hume-Ruthery [248] for the solid solutions and hence cross-substitution (both the sites Sr and Ce) of Gd^{3+} might be possible. The reason for no significant change in the position of XRD peaks of the samples x = 0.04, 0.06 and 0.10 might be due to the cross-substitution of Gd^{3+}. From this result one may infer that in the sample SCG2 (x=0.02) Gd^{3+} ions substitute at Ce^{4+} - site. However, in higher concentration solid solutions i.e. samples with x =0.04, 0.06 and 0.10, Gd^{3+} ions partially substitute at Sr^{2+} sites. Sharing of Ba and Ce/Ti sites by the dopant Gd in perovskite oxides $BaCeO_3$ and $BaTiO_3$ has been reported [249].To determine value of the lattice parameters, Rietveld refinement was performed to the XRD data. Rietveld refinement was carrying out by FullProf software. For Rietveld refinement distorted orthorhombic crystal

structure and space group Pnma reported in the literature for $SrCeO_3$ [250] were considered. The XRD patterns observed experimentally, calculated theoretical and their difference all the samples are illustrated in **Figure 5.2**. In **Figure 5.2**, a reasonable matching between observed and calculated XRD patterns even for the doped samples is seen. This means that substitution of Gd has not produced any structural transformation. Values of the lattice parameters, cell volume and reliability factors for all the samples are presented in Table 5.1. The agreement factors are quoted using x^2 statistics and the *R* factors, *R,* (profile), *R,* (weighted profile) and *R,* (structure factor). These are defined in Table 5.1, where details pertaining crystal data, data collection and structure refinement are listed. Profile plots are shown in **Figure 5.2**.

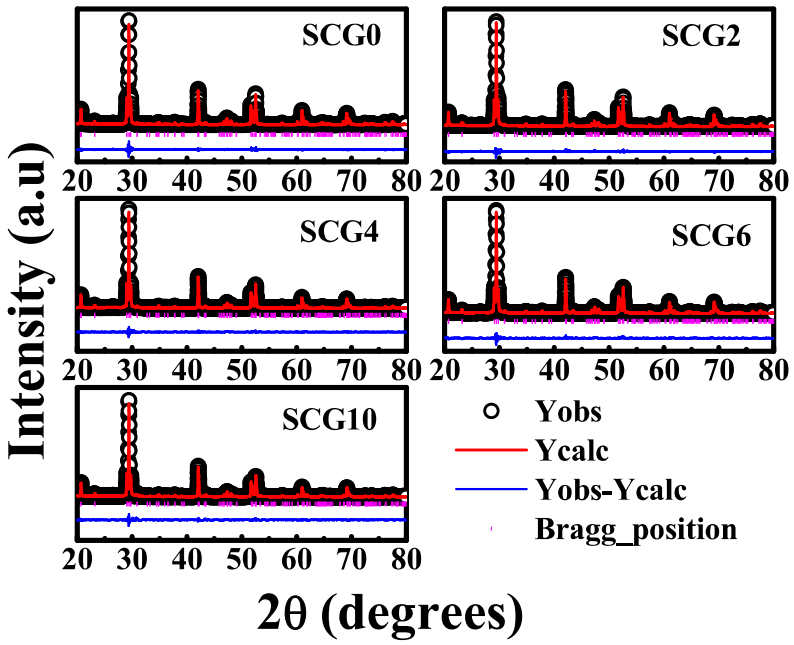

Figure 5.2 Rietveld refinement of X-ray diffraction pattern of samples in the system $SrCe_{1-x}Gd_xO_4$.

Values of the lattice parameters for undoped sample $SrCeO_3$ (SCG0) are in agreement with previously reported values [250]. From the Table 5.1, it seen that lattice parameter a and b increases with increasing x whereas lattice parameter c decreases with increasing x. The cell volume remains almost same for all the samples. As pointed out by McBride et al, the resulting

parameters under doping is not determined solely by the ionic radius. Coulomb effects, oxygen vacancies, and changes in the force constants introduced by doping may also play important roles. In fact, our results are in good agreement with the one obtained by Wang et al. for Gd doped $BaCeO_3$ who observed very small variations in the cell dimension as a consequence of doping Ceria with Gd.

Size Strain Plot (SSP) method has been used to evaluate the crystallite size and strain [247]. The advantage of this method is that it gives less weightage to the data of reflection arises from higher angles where precession is lower. Therefore, Size Strain Plot (SSP) method has been used to determine the crystallite size and lattice strain in the synthesized samples. According to SSP plot method, interplanar spacing and strain is related as per **Eq. (5.1)**

$$\left(\frac{d_{hkl}\beta\cos\theta}{\lambda}\right)^2 = \frac{k\lambda}{D}\left(\frac{d_{hkl}^2\beta\cos\theta}{\lambda^2}\right) + \left(\frac{\varepsilon}{2}\right)^2 \quad (5.1)$$

Where, d_{hkl} is the interplanar spacing corresponding to the plane (hkl), D crystallite size, k is the Scherer's constant = 0.9 for spherical particles, λ is the wavelength of X-ray and ε is the average strain generated in the lattice.

Table 5.1 Various parameters obtained from Rietveld refinement analysis of XRD data of the prepared system $SrCe_{1-x}Gd_xO_3$ ($0.00 \leq x \leq 0.10$).

Samples	Atoms	Positions			R-factor				Lattice Parameters (Å)	Cell Volume (Å^3)
		x	*y*	*z*	R_p	R_{wp}	R_f	χ^2		
SCG0	*Sr (4c)*	0.455	0.250	0.008	4.31	4.35	4.03	1.30	a = 6.1487 b = 8.5815 c = 6.0069	316.30
	Ce (4b)	0.000	0.000	0.000						
	OI (4c)	0.533	0.250	0.599						
	OII(8c)	0.201	0.056	0.301						
SCG2	*Sr (4c)*	0.456	0.250	0.009	4.41	4.8	3.99	1.54	a = 6.1489 b = 8.5826 c = 6.0068	316.97
	Ce (4b)	0.000	0.000	0.000						
	Gd(4b)	0.000	0.000	0.000						
	OI (4c)	0.546	0.250	0.599						
	OII(8c)	0.208	0.061	0.300						
SCG4	*Sr (4c)*	0.457	0.250	0.013	4.32	4.38	3.86	1.75	a = 6.1495 b = 8.5834 c = 6.0063	317.03
	Ce (4b)	0.000	0.000	0.000						
	Gd(4b)	0.000	0.000	0.000						
	OI (4c)	0.530	0.250	0.605						
	OII(8c)	0.205	0.057	0.304						
SCG6	*Sr (4c)*	0.450	0.250	0.014	3.92	4.26	4.08	1.69	a = 6.1513 b = 8.5845 c = 6.0047	317.08
	Ce (4b)	0.000	0.000	0.000						
	Gd(4b)	0.000	0.000	0.000						
	OI (4c)	0.549	0.250	0.618						
	OII(8c)	0.209	0.058	0.305						
SCG10	*Sr (4c)*	0.457	0.250	0.013	3.85	4.77	4.00	1.80	a = 6.1530 b = 8.5859 c = 6.0024	317.10
	Ce (4b)	0.000	0.000	0.000						
	Gd(4b)	0.000	0.000	0.000						
	OI (4c)	0.550	0.250	0.616						
	OII(8c)	0.208	0.057	0.298						

The plot of $\left(\frac{d_{hkl}\beta cos\theta}{\lambda}\right)^2$ vs.$\left(\frac{d_{hkl}^2\beta cos\theta}{\lambda^2}\right)$ for all the samples are shown in **Figure 5.3**. By linear fitting of the experimental data points, the value of slope and intercept on y-axis was obtained. The value of crystalline size is calculated from the slope. Whereas, square root of the intercept was used to obtained the value of lattice strain. The values of crystallite size and lattice strain of various compositions are mentioned in Table 5.2. It is noticed from the Table 5.2 that crystallite size increases with increasing Gd upto x = 0.06 (SCG6) thereafter it has decreased for sample with x=0.10 (SCG10). Lattice distortion is also highest for sample the samples with x=0.06.

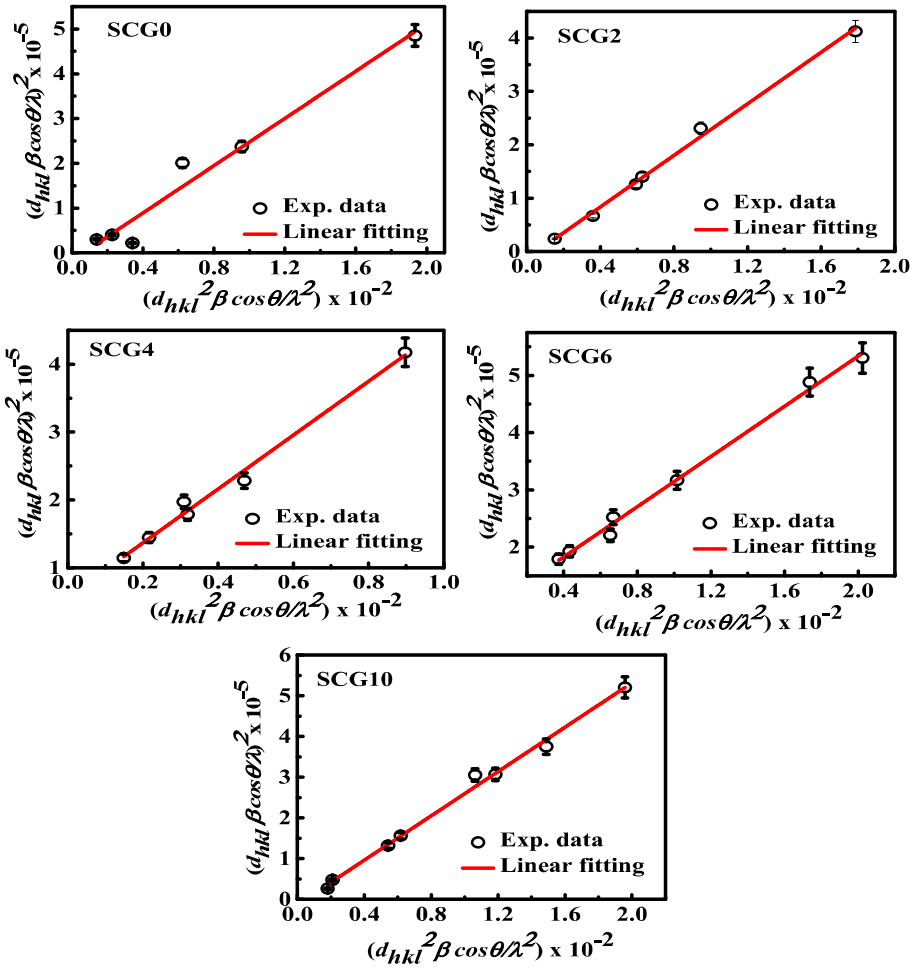

Figure 5.3 Size Strain plots (SSP) for determination of crystalline size and lattice strain of the samples.

Table 5.2 Crystallite size, lattice strain determined from size strain plots (SSP) method, optical band gap from Tauc plots, average grain size, electrical conductivity and activation energy of the prepared system $SrCe_{1-x}Gd_xO_3$ ($0.00 \leq x \leq 0.10$).

Sample Code	Crystallite size (nm)	Lattice strain (ε)x10^{-3}	Optical band Gap (eV)	Average grain size (µm)	Electrical Conductivity ($S.cm^{-1}$) at 460 °C	Activation Energy (eV) 300 – 600 °C
SCG0	58.84	2.47	3.00	1.41	6.79 x 10^{-6}	0.89
SCG2	60.09	2.29	2.99	1.46	1.24 x 10^{-3}	0.80
SCG4	72.76	4.79	2.80	1.23	3.20 x 10^{-4}	0.76
SCG6	66.12	6.17	2.94	1.03	1.16 x 10^{-5}	0.88
SCG10	53.24	2.24	2.81	0.96	7.46 x 10^{-7}	0.94

5.3.2 Raman spectra analysis

Raman spectrometry serves as an effective tool to probe local symmetry of the crystalline materials. This technique also provides information about structure, phase and purity/quality of the synthesized powders and formation of defects such as oxygen vacancies. A through literature survey has indicated that synthesis of hundred percent pure powder of $SrCeO_3$ by any method is challenging. Powders of $SrCeO_3$ very often contain trace amount of impurity phases CeO_2, $SrCO_3$ and Sr_2CeO_4. Detection of these phases in the powder of $SrCeO_3$ by conventional powder XRD is difficult because of two reasons; firstly, due to superposition

of peak position of $SrCeO_3$ and impurity phases and secondly due to presence of impurity phases in trace about i.e. below the detection limit. These impurities phases can be detected precisely using Raman spectroscopy because position of strongest Raman band of above-mentioned impurity phases is entirely different than the Raman band of $SrCeO_3$. Thus, to check the purity of the synthesized powders, distortion in the local symmetry and presence of oxygen vacancies, Raman spectra of the samples were recorded in the wide range of the wave number 100 – 750 cm^{-1}. The room temperature Raman spectra of the samples are illustrated in **Figure 5.4**. Raman spectra of all the samples show a characteristic band for perovskite structure $SrCeO_3$ around 344 cm^{-1} [225]. The intensity of the bands in each spectrum was normalized by an intensity of a main band at about 344 cm^{-1}. No obvious shift in the strongest Raman band (at 344 cm^{-1}) on doping Gd was observed. The influence of Gd^{3+} doping is observed in the broadening of 344 cm^{-1} Raman band. This broadening is probably induced by local distortion around the Gd^{3+} ions. This is because in $SrCeO_3$ perovskite structure only oxygen atoms can move, and hence the frequency of this band should be independent of the cation mass [13]. Besides, the typical Raman bands of $SrCeO_3$ at 110, 124, 147, 180, 240, 281, 320, 348, 378, 409, 462,525, 643 [225], a weak intensity band at 462 cm^{-1} is seen in the spectrum of all the samples, which is attributed to F_{2g} band of CeO_2 [251]. A very weak and broad band around 704 cm^{-1} is also present in the spectrum of all the samples which is assigned $SrCO_3$ [251]. Three prominent Raman bands of Gd_2O_3 are reported at 314, 359 and 446 cm^{-1} [251]. Absence of these vibrational bands (even strongest one at 359 cm^{-1}) in the Raman spectra of Gd doped samples implies that Gd_2O_3 does not exist as separate phase. Two strongest Raman bands at 286 and 385 cm^{-1} of commonly found secondary phase Sr_2CeO_4 were not seen in the Raman spectra of the samples [252].

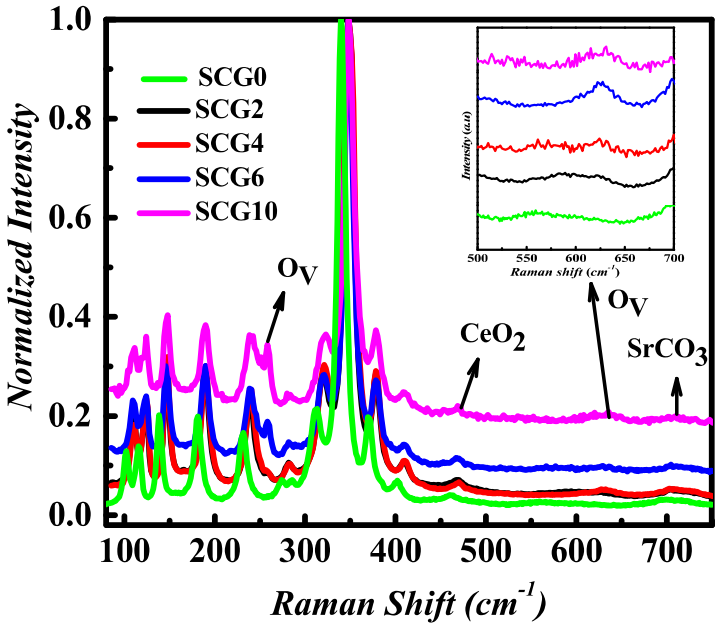

Figure 5.4 Room temperature Raman spectra of all prepared samples.

Besides, the above mentioned characteristic bands of $SrCeO_3$, $SrCO_3$ and CeO_2, a hump in the Raman spectrum of undoped sample at 569 cm^{-1} appeared which is attributed to oxygen vacancies (intrinsic) generated on reduction of Ce^{4+} to Ce^{3+} in $SrCeO_3$. In the Raman spectra of doped samples, intensity of this hump decreases with increasing, x and in the samples SCG6 and SCG10 completely disappeared. This result, allows us to conclude that doping of Gd^{3+} at Ce^{4+} site of $SrCeO_3$ has suppressed reduction of Ce^{4+} into Ce^{3+}.

The Raman spectra of doped samples contain two more additional bands at 253 and 630 cm^{-1}. The intensity of bands gradually increases with increasing dopant concentration of Gd, strongly suggesting that these bands are due to vibration modes involving the dopant ion (Gd). In the Raman spectra of Gd-doped CeO_2 systems also bands around 253 cm^{-1} and 550-600 cm^{-1} have been reported and correlated with formation of associate defects and oxygen vacancies [253]. Furthermore, in acceptors (Yb, Gd and Nd) doped $BaCeO_3$ and $SrCeO_3$ systems also a broad band in the range 600-650 cm^{-1} has been is recorded and assigned to oxygen vacancies

[253]. Oxygen vacancies in doped samples, generated as charge compensation defects in the crystal lattice of $SrCeO_3$ to maintain the charge neutrality when Ce^{4+} ions are replaced by Gd^{3+} ions. Presence of two bands at 253 and 630 cm^{-1} in the Raman spectrum of doped samples is a signature of existence of oxygen vacancies (extrinsic) in the samples due to incorporation of Gd^{3+} in the crystal lattice of $SrCeO_3$. We will describe the mechanism of generation of intrinsic and extrinsic oxygen vacancies in the samples in subsequent section on electrical properties.

5.3.3 FTIR analysis

Studies on perovskite oxides based alkaline earth titanates and stannates have shown that Fourier Transform Infrared (FTIR) technique is very useful in detecting alkaline earth carbonates commonly present in the synthesized powders. This technique can detect very low ($\leq 0.6\ \%$) concentrations of alkaline earth carbonates. Hence, to check the presence of impurity phase SrCO3 in the synthesized samples FTIR, spectra of the samples was recorded and shown in **Figure 5.5**. An incomplete broad band in the range of 500 to 540 cm^{-1} is observed in the spectrum of all the sample. This band is assigned to the Ce-O stretching vibration band in CeO_6 octahedra, which confirmed $SrCeO_3$ type structure of all the samples in agreement with XRD and Raman results. Absence of most strongest FTIR band of Gd-O vibration in cubic Gd_2O_3 at 583 cm^{-1} again confirmed incorporation of Gd^{3+} in the lattice of $SrCeO_3$ in doped samples [251]. The characteristic bands of $SrCO_3$ at 699, 706, 860, 1070, 1453 and 1768 cm^{-1} are also seen in the spectra of the samples [254]. From the **Figure 5.5** it is noted that intensity of band at 1453 cm^{-1} increases with increasing dopant (Gd) concentration. Higher intensity of the carbonate bands in sample SCG10, indicates larger amount of $SrCO_3$ in this composition. Another weak intensity band observed at 2361 cm^{-1} suggests presence of CO_2 gas in the sample may be due to adsorption of CO_2 from the air during the measurement [255]. It is possible that the formation of $SrCO_3$ in the samples have been taken placed during the experiment by adsorbing CO_2 on the surface of the samples. Adsorption on the surface depends on the particle

size and among all the synthesized samples, sample SCG10 has smallest particle size and hence adsorption of CO2 on the surface of this sample is expected to be higher than the other samples. A broad band in the range 3250 – 3525 cm-1 is characteristic of O-H stretching vibration of surface hydroxyl group due to adsorption of water molecules from the air [256]. Using FTIR it is tedious to quantify amount of SrCO3 phase in the synthesized powders. To quantify the amount of this phase thermal analysis technique has been used and results are discussed in detail in the next section.

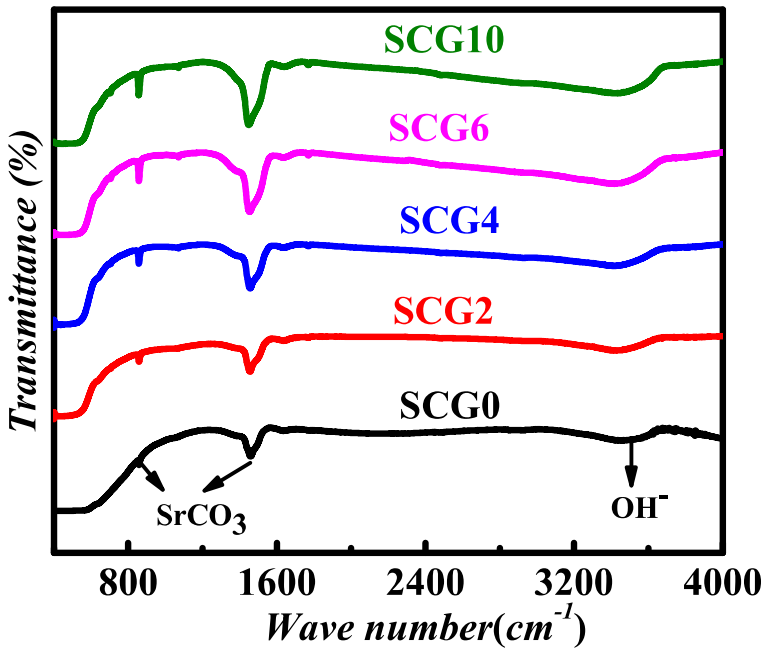

Figure 5.5 Fourier transformed infra-red (FTIR) spectra of all prepared samples.

5.3.4 Thermal analysis (TGA/DSC)

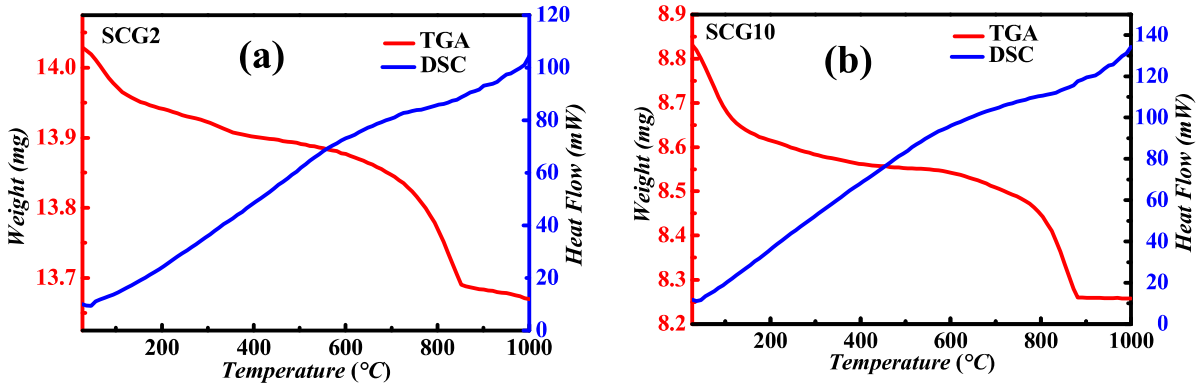

Figure 5.6 Thermo gravimetric analysis (TGA) and differential scanning calorimetric (DSC) curves.

Figure 5.6 (a) - (b) show thermogravimetric (TG) and differential scanning calorimetry (DSC) curves for two representative samples SCG2 and SCG10, respectively. Similar curves were recorded for other samples also. A total weight loss of 2.55 % and 6.43 % was observed for SCG2 and SCG10 in two steps RT-200 ^{o}C and 600-900^{o}C. First step weight loss is attributed to removal of water adsorbed from the atmosphere. Second step weight loss between 600 - 900^{o}C is associated with decomposition of $SrCO_3$ [257]. Higher weight loss in the second step for SCG10 (3.24 %) as compared to SCG2 (1.32%) may be due to smaller particle size of SCG10 than SCG2. Smaller grain size and hence higher surface area can be responsible for higher amount of water molecules and CO_2 gas adsorption from the atmosphere. Raman studies have also indicated presence of $SrCO_3$ in the synthesized samples but in the XRD no peak corresponding to $SrCO_3$ was detected. The reason for this is that amount of $SrCO_3$ in SCG10 sample is approximately 3 weight %. It is known that detection limit of conventional XRD is >3 weight %, therefore in the XRD, no peak corresponding to $SrCO_3$ phase was detected. In the DSC plots no endothermic and exothermic peak was detected which rules out formation any new phase.

5.3.5 UV–Visible analysis

To study the influence of Gd doping on the optical band gap of $SrCeO_3$, UV-visible spectra of all the samples has been recorded and depicted in **Figure 5.7**. As can be noted from this figure, the major UV-vis absorption for spectra occurs at about 221, 258, and 315 nm. The former maxima (221 nm) correspond to O_2 - to Ce^{3+} charge transfer transitions, whereas the latter two absorption maxima may be caused by O_2 - to Ce^{4+} charge transfer (258 nm) and interband (315 nm) transitions. O_2 - to Ce^{3+} and O_2 - to Ce^{4+} are defect bands or states .They will have either lower energy or same as bandgap. On careful observation of the absorption spectra it was noticed that the position of broad band around 315 nm has slightly shifted (315 nm to 320 nm) towards higher wavelength side with increasing Gd concentration. Change in the position of absorption peak with increasing Gd concentration confirmed incorporation of Gd at the lattice positions in the structure of $SrCeO_3$. Further, it is observed that absorption at peak position for doped samples is approximately 90 % higher than undoped sample $SrCeO_3$ (84 %). On the contrary, absorption in the visible range (450 -700 nm) of doped samples is (5 %) less than that of undoped sample (11 %).

The band gap energy of the samples was calculated from their absorption curves, using Tauc's relation given by **Eq. (5.2)**;

$$(\alpha h\vartheta)^{1/\gamma} = A\left(h\vartheta - E_g\right) \tag{5.2}$$

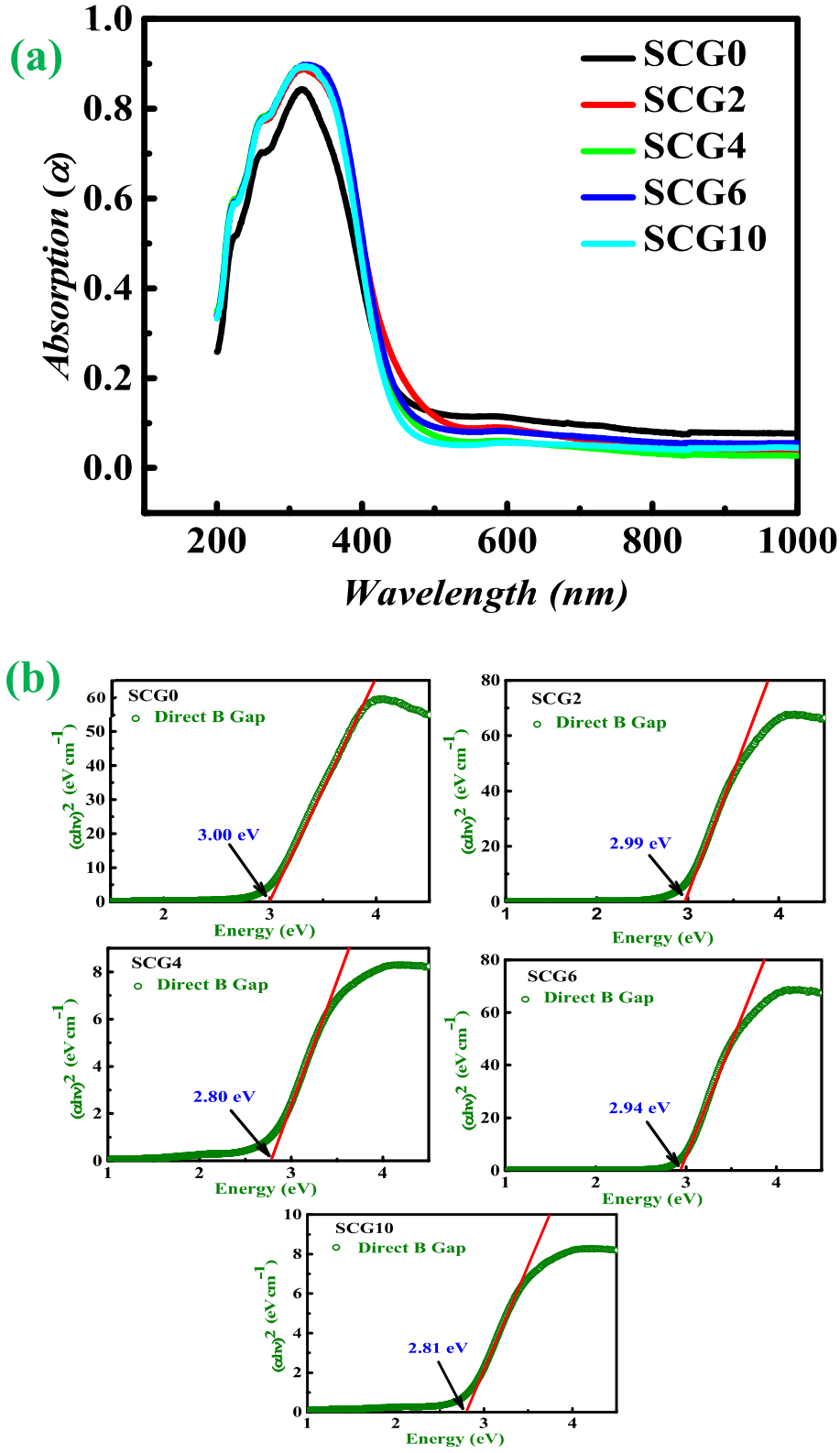

Figure 5.7 (a) UV- visible absorption spectra and **(b)** Tau plots received from the absorption data *of* the prepared system $SrCe_{1-x}Gd_xO_3$ ($0.00 \leq x \leq 0.10$).

Where E_g is the optical band gap, h the Planck's constant and ν the frequency of incident photons, A is a constant called the band tailing parameter, and γ is the index. The value of exponent γ represents the nature of the optical transitions, γ = 1/2, 2, 3/2, 3 denote for direct allowed, indirect allowed, direct forbidden and indirect forbidden transitions respectively. Tauc plots for direct allowed transition, plotted between photon energy (hν) on x-axis and $(\alpha\ h\ \nu)^2$ on y-axis [247] for different samples, are shown in **Figure 5.7 (b)**. These plots were used to determine the band gap in electron volt (eV) of different samples. The value of Band gap (E_g) energy obtained from Tauc plots is listed in Table 5.2. The obtained value of the direct band gap of $SrCeO_3$ is in accordance with value reported in the literature [247]. Form the data presented in Table 5.2, it is clear that as the doping concentration of Gd increases optical band gap decreases. The decreasing or increasing the bandgap energy with doping depends also on the lattice distortion. In case of perovskite materials, the doping sometimes leads to increase the octahedral distortion resulting in decreasing bandgap. The decrease in the value of energy gap (red shift) confirmed the replacement of Ce^{4+} ions by Gd^{3+} ions.

5.3.6 Microstructural and energy dispersive x- ray analysis

For the electrical characterization, calcined powders were pelletized and sintered at 1200°C for 12 h. In the literature need of high temperature sintering (≥1400°C) to achieve dense ceramic of $SrCeO_3$ has been mentioned [258]. But due to unavailability of furnace (working temperature ≥1400°C), samples were sintered at 1200°C. The surface morphology of the fractured surfaces of sintered samples has been studied using scanning electron microscopy (SEM), **Figure 5.8** displays the SEM images of the samples. The SEM images of all the samples contain grains of spherical shape. A wide dispersion in the grain size is seen in the SEM images. A histogram to show the distribution in the grain size of the samples has been

generated by **Image J** software. To obtain value of the average grain size, the Gaussian function was fitted to generate histograms (see **Figure 5.9**). The value of average grain size of all the samples is listed in Table 5.2. It is observed from the Table 5.2 that average grain size of the samples with x= 0.02 and (SCG2) is slightly larger than that of undoped sample $SrCeO_3$ (SCG0). However, as doping concentration increases ($x \geq 0.04$) a progressive decrease in the grain size is observed. Smaller grain size of the samples with higher concentration of dopant Gd may cause by segregation of impurities such as SrO or additive Gd_2O_3 at the grain surfaces and grain boundaries. On careful observation of micrograph of sample SCG10 it is found that small size spherical grains having slightly different colour are homogeneously distributed at the grain boundaries in the micrograph of sample SCG10. These grains may belong to SrO/Gd_2O_3. In solid solutions $SrCe_{1-x}Gd_xO_3$, if Gd ions occupy Sr sites instead of targeted site Ce^{4+}, replaced Sr ions can form SrO and segregate at the grain boundaries. It is well known that SrO is very reactive to CO_2 present in the atmosphere and get convert into $SrCO_3$. Presence of $SrCO_3$ in the synthesized samples have been detected from the results of Raman, FTIR and TGA measurements. These techniques have not indicated presence unreacted Gd_2O_3 in the samples. Therefore, small size grains belongs to $SrO/SrCO_3$, whereas the large size grains are identified to be the perovskite phase of $SrCe_{1-x}Gd_xO_3$. Further, it was clearly observed that amount of residual SrO increases with increasing Gd concentration in the solid solution.

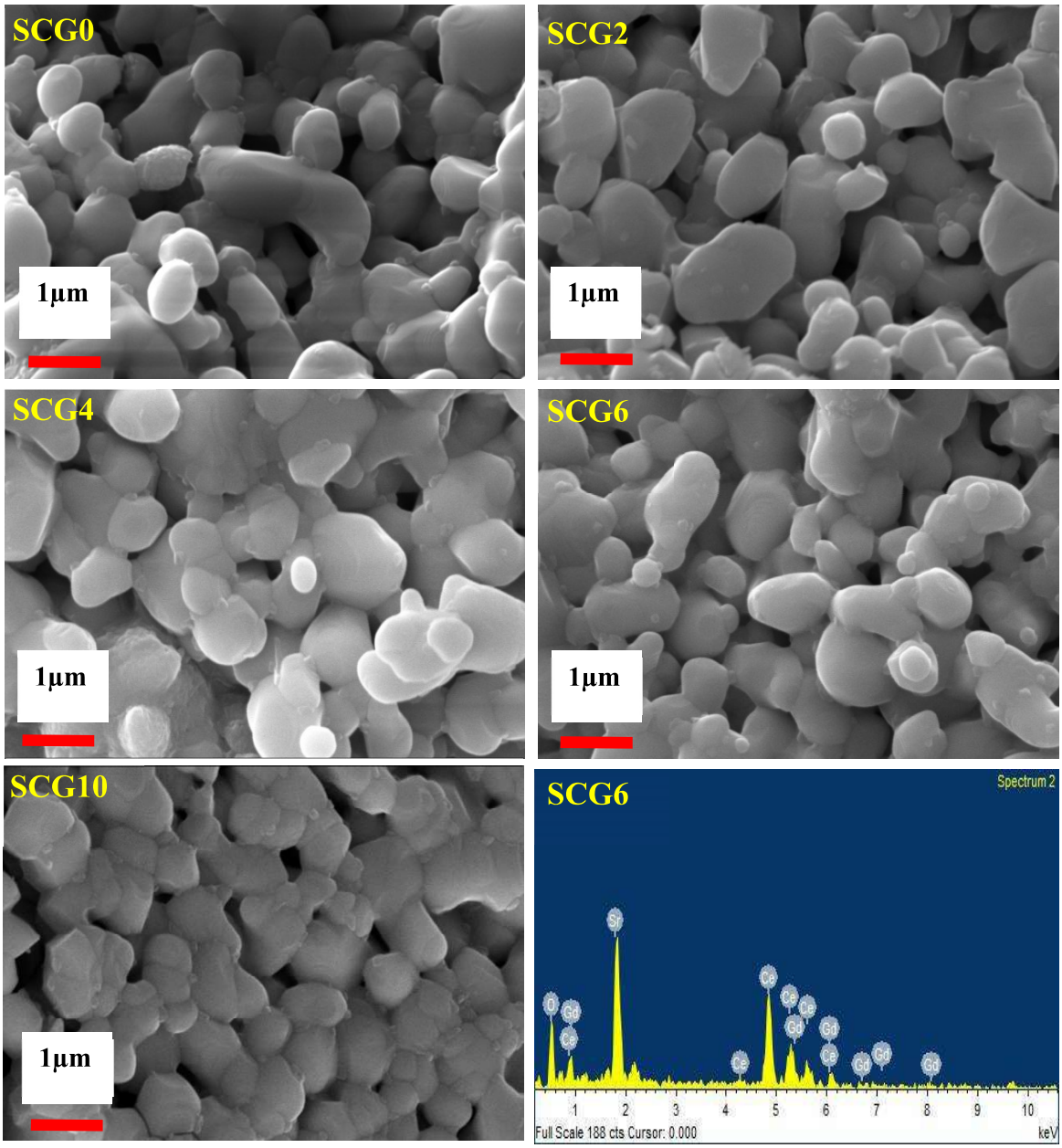

Figure 5.8 Scanning electron micrograph (SEM) of fractured surfaces and EDX spectrum.

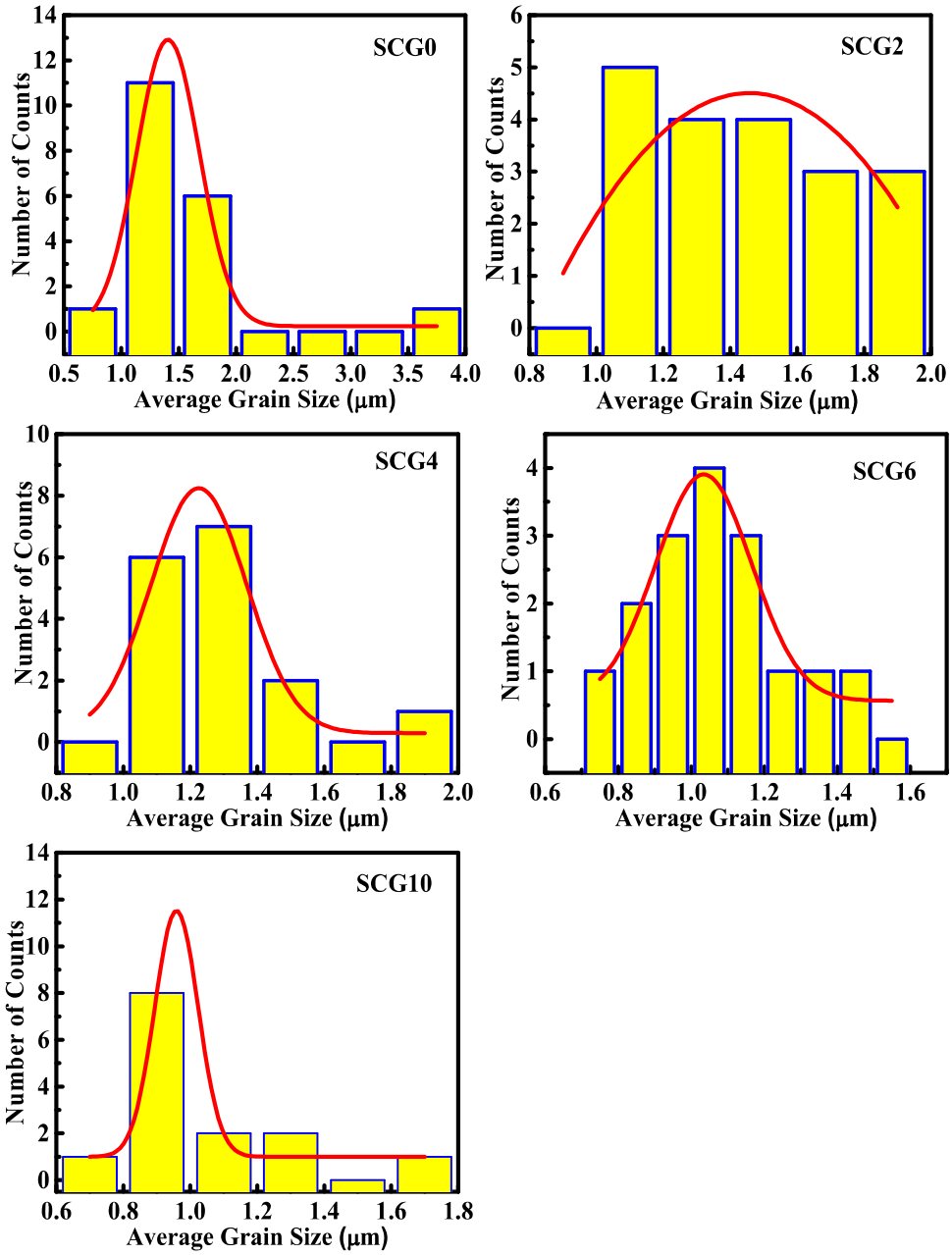

Figure 5.9 Histograms of distribution in grain size of the samples.

5.3.7 Impedance spectroscopy

Complex plane impedance analysis has been employed widely to study electrical properties of polycrystalline materials. Prime goal of using impedance analysis is to separate the contribution of grains, grain boundaries and electrode/sample interface resistance to the total resistance [250]. Hence, complex plane impedance plots of the samples were generated using measured values of resistance and capacitance in temperature range 300 – 600 ^{o}C and frequency range 20 Hz – 2 MHz. Typical complex plane plots of sample $SrCe_{0.90}Gd_{0.10}O_3$ (SCG6) at few selected temperatures are shown in **Figure 5.10**. Similar plots were observed for other samples. Impedance plot at different temperatures exhibit a small arc in lower frequency range followed by a depressed semicircular arc in the high frequency range. The observed semicircular arc in higher frequency range can be associated with grains or grain boundaries. Assignment of observed arc to grains and grain boundaries can be made by determining capacitance from the relation $2\pi f_{max}RC = 1$, where f_{max} is the frequency of applied single at the arc maximum and R is the resistance and C is the capacitance of a particular contribution. The capacitance corresponding to semi-circular arc has been calculated. The value of capacitance is found to be of the order of 10^{-11} F. The grains and grain boundaries arcs are associated with capacitances in the pF (10^{-12} – 10^{-10} F) and nF (10^{-9} – 10^{-8} F) ranges. Therefore, the observed high frequency arc is assigned to grains contribution. Values of bulk resistance at different temperatures were determined by fitting nonlinear curve to the impedance plots shown in **Figure 5.10**.

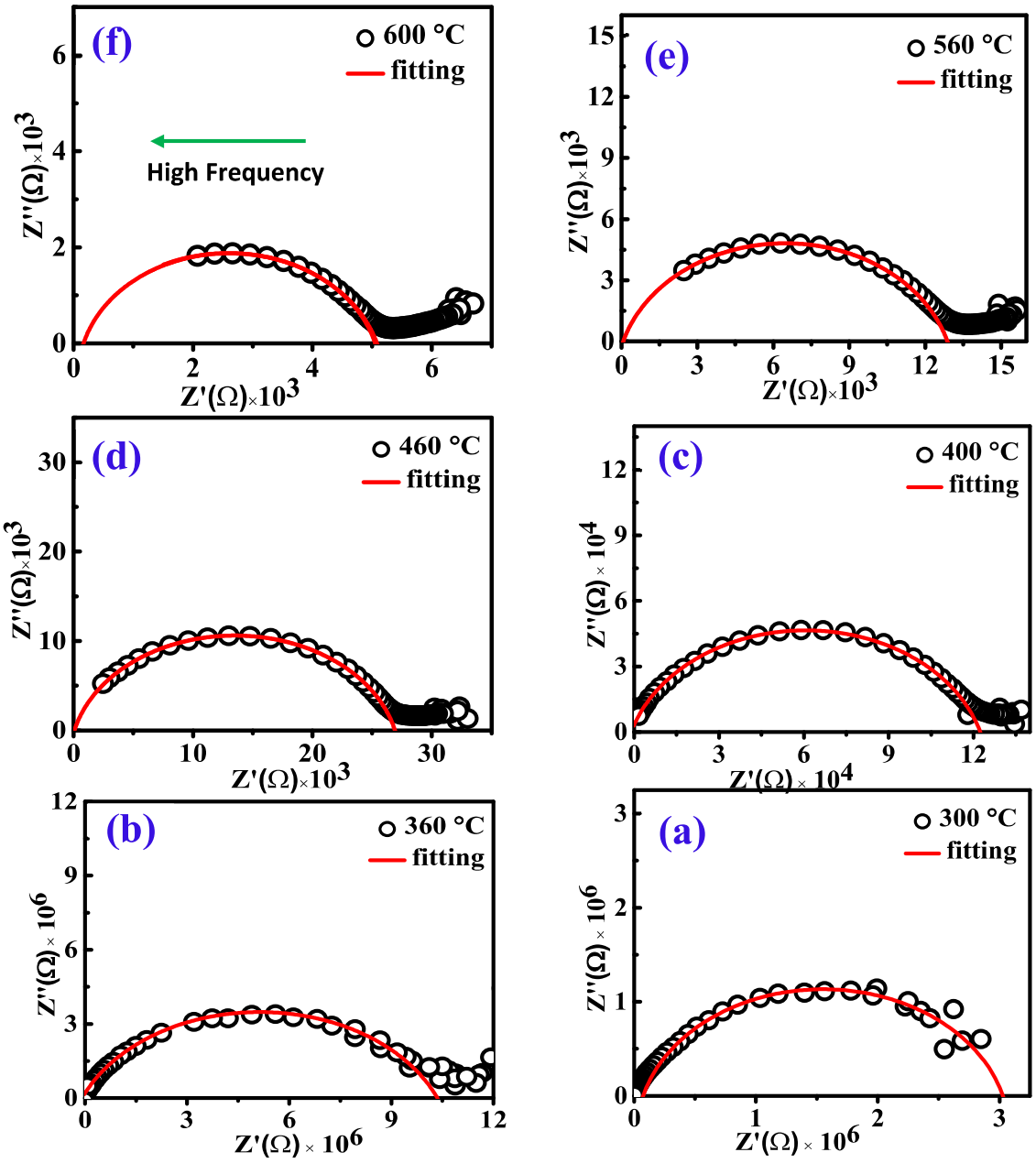

Figure 5.10 The complex plane impedance plots for the composition SCG6: **(a)** 300 °C, **(b)** 360 ° C, **(c)** 400 °C, **(d)** 460 °C, **(e)** 560 °C and **(f)** 600 °C.

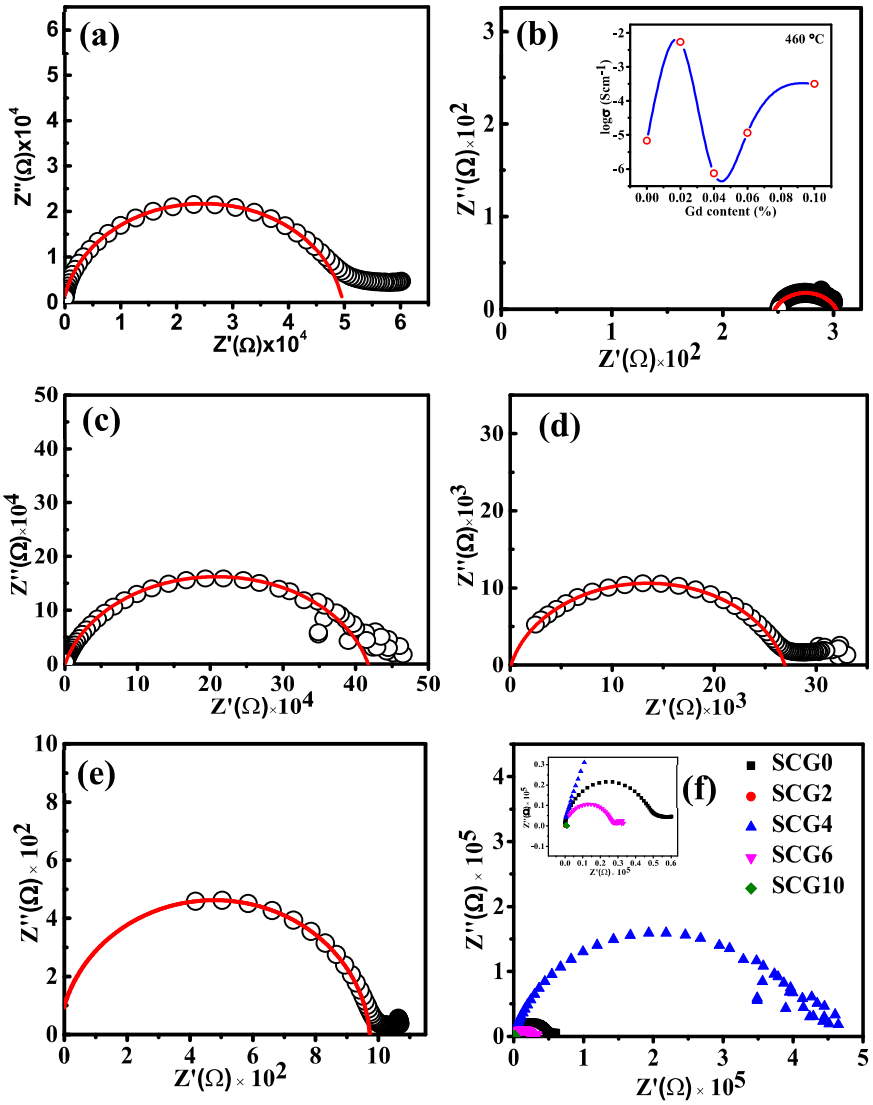

Figure 5.11 The complex plane impedance plots for compositions: **(a)** SCG0 **(b)** SCG2, **(c)** SCG4 **(d)** SCG6 **(e)** SCG10 and **(f)** combined plot for $SrCe_{1-x}Gd_xO_3$ ($0.00 \leq x \leq 0.10$): at 460 °C.

In order to show the variation of impedance of all composition of prepared system, the complex plane impedance plots with nonlinear curve fitting are depicted in **Figure 5.11 (a) - (f)**. Where this show the separate plots for each composition of prepared system at 460 ºC and **Figure 5.11 (f)** represents the combined plots. **Figure 5.11** clearly indicates that the sample SCG2 has the lowest impedance.

Bulk conductivity (σ) has been calculated using the formula:

$$\sigma = \frac{1}{R} \times \frac{L}{A} \tag{5.3}$$

Where, L is the thickness and A is the surface area of pellet, R is the bulk resistance. **Figure 5.12** shows the plots of $log\ \sigma$ versus $1000/T$ for all the samples. Activation energy of the bulk conduction was estimated by fitting the data in **Figure 5.12** to Arrhenius relationship:

$$\sigma = \sigma_o\ exp\left[-\frac{E_a}{kT}\right] \tag{5.4}$$

Where σ_o, k, T and E_a are the pre-exponential factor, Boltzmann constant, absolute temperature, association energy, respectively. Values of activation energy calculated from the slopes and given in Table 5.2. These values of activation energy are found to agree with the values reported for oxygen vacancies conduction in perovskite oxides and fluorite CeO_2 [259]. In these samples generation of oxygen vacancies may occur in two ways: (i) to compensate reduction of Ce^{4+} into Ce^{3+} named as intrinsic oxygen vacancies and (ii) due to substitution of lower valent ion Gd^{3+} at Ce^{4+}, named as extrinsic oxygen vacancies. The probable reaction of intrinsic and extrinsic oxygen vacancies generation are written in Kronger Vink notation:

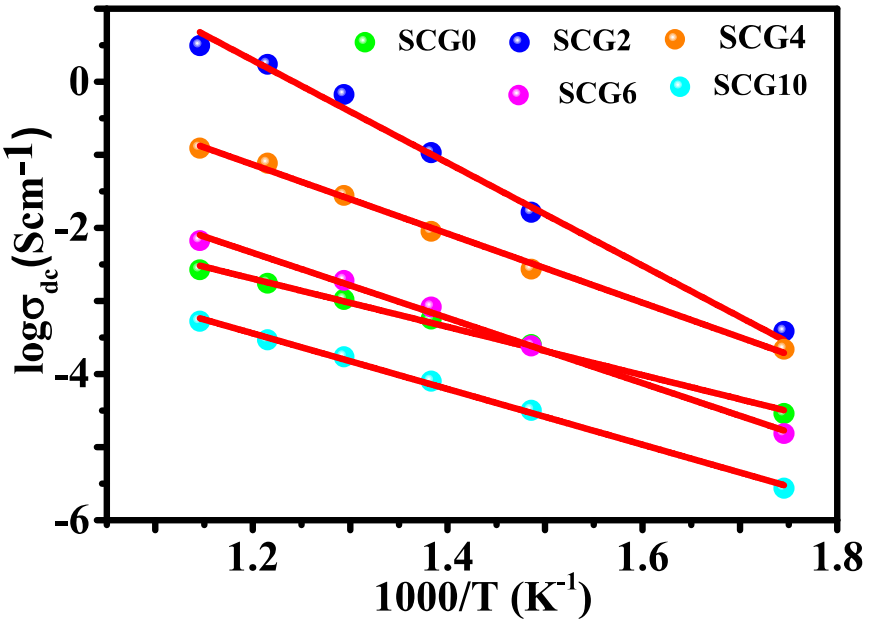

Figure 5.12 Bulk conductivity of the samples in the system $SrCe_{1-x}Gd_xO_3$.

$$Ce_2O_3 \xrightarrow{2SrCeO_3} 2Ce_{Ce}{}' + V_{\ddot{O}} + 3O_0{}^x + \frac{1}{2}O_2(g) \quad (5.5)$$

$$Gd_2O_3 \xrightarrow{2SrCeO_3} 2Gd_{Ce}{}' + V_{\ddot{O}} + 3O_0{}^x + \frac{1}{2}O_2(g) \quad (5.6)$$

Activation energies for oxide-ion transport in $SrCeO_3$-based systems determined experimentally range from 0.67 to 0.77 eV [238, 260] in the temperature range 600-800 °C. Slightly higher value of activation energy in this work may be due to higher porosity on account of lower sintering temperature. Activation energy for $SrCe_{0.95}Gd_{0.05}O_{2-975}$ is reported to be 0.64 eV [238]. Value of activation energy is lowest for sample SCG4 (0.76 eV) and highest for SCG10 (0.94 eV). In higher dopant concentration samples, most of the oxygen vacancies are bound with the negatively charge sites occupied by dopant cations. Activation energy for higher concentration samples is sum of association energy and migration energy while in lower concentration it is equal to the activation energy of migration only.

The total conductivity at 460°C of all the samples is tabulated in Table 5.2. It is observed from the Table 5.2 that sample with x=0.02 (SCG2) has highest value of the conductivity 1.24×10^{-3} Scm^{-1}. Value of conductivity of sample x=0.06 (1.16×10^{-5} Scm^{-1}) is consistent with value 5.49×10^{-5} Scm^{-1} reported for $SrCe_{0.95}Gd_{0.05}O_{2.975}$ [238]. Concentration of oxygen vacancies increases with increasing x i.e. concentration of Gd. The mobility of $V_O^{\bullet\bullet}$ is generally believed to depend on the crystal structure, type of dopant, and association among defects. As dopant concentration increases, the probability of the formation of associate defect pairs $(2Gd'_{Ce} - V_O^{\cdot\cdot})^{\times}$ also increases. Possible reasons for the higher value of activation energy and lower value of conductivity of high concentration Gd samples are as follows:

(i) Formation of associate defects in the samples SCG6 and SCG10 can be attributed to formation of associate defects. It is already discussed that in the Raman spectrum of samples SCG6 and SCG10, a new band at 253 cm^{-1} is signature of existence of associate defects in these samples.

(ii) Segregation of SrO at grain boundaries and triple points.

(iii) Significant grains separation that higher value of porosity.

(iv) Decreasing grain size with increasing, x.

5.3.8 X-ray photoelectron (XPS) measurements

In Ce based compounds existence of Ce in mixed valence state is very common. Therefore, X-ray photoelectron spectroscopy (XPS) measurements were carried out to reveal the valence state of Ce cation and verify the existence of oxygen vacancy in the samples. The high-resolution x-ray photoelectron spectrum (HRXPS) of Ce 3d and O 1s core level spectra were recorded for one of the representative samples SCG4 (with x=0.04) and shown in **Figure 5.13**. The core-level (CL) peaks were fitted after Shirley background subtraction using Voigt (mixed Lorentzian–Gaussian) line shape calibrated against C (1*s*) having a binding energy of 284.8 eV for surface contamination layer. **Figure 5.13 (a)** shows core level spectrum of Ce. The peaks observed at particular binding energies were matched with binding energy value for Ce^{3+} and Ce^{4+} reported in the literature [261]. Presence of four prominent peaks of Ce^{4+} $3d_{3/2}$

(916.8), Ce^{4+} $3d_{5/2}$ (898.1), Ce^{3+} $3d_{3/2}$ (900.7) and Ce^{3+} $3d_{5/2}$ (882.3) for sample SCG4 has clearly demonstrated existence of Ce in both Ce^{3+} and Ce^{4+} states. The peak areas of Ce^{3+} total areas ratio was used to calculate the relative amount of Ce^{3+}. However, it is difficult to obtain a concrete value due to the complex backgrounds.

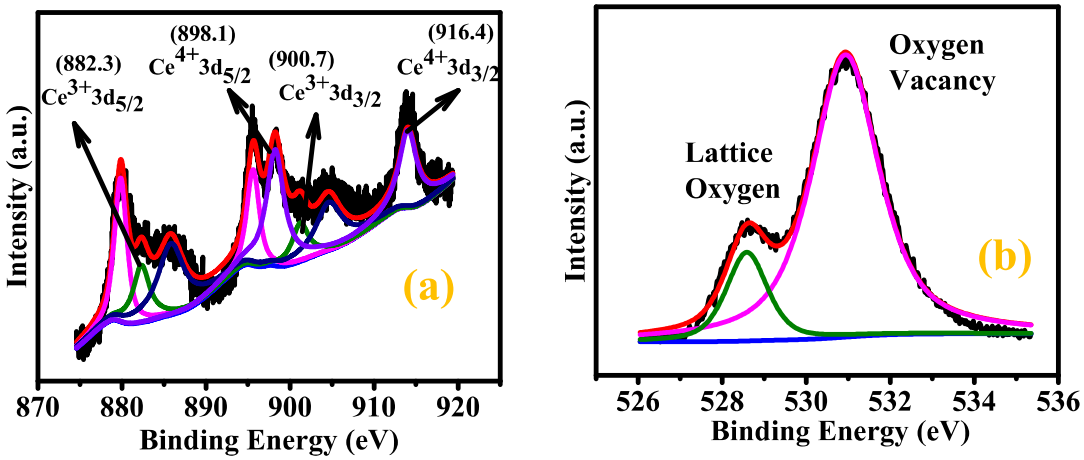

Figure 5.13 (a) Deconvoluted XPS of Ce 3d profile **(b)** of O 1s profile of sample $SrCe_{0.96}Gd_{0.04}O_3$ (SCG4).

Figure 5.13 (b) shows XPS spectrum of O 1*s*; two well resolved peaks at 528.6 eV and 531 eV. The lower binding energy (528.6 eV) peak is associated with lattice oxygen, whereas the higher binding energy (531 eV) normally corresponds to oxygen vacancies [262]. Higher intensity of peak corresponding to oxygen vacancies than for lattice oxygen suggest that large number of oxygen vacancies at the surface of synthesized sample SCG4. It is known that XPS is a surface technique that is highlights information about surface properties. Higher concentration of oxygen vacancies at the surface of the synthesized samples may arise due to inhomogeneous distribution of Gd (Gd substitution is higher at the outer surface than at the internal layers). The activation energy for diffusion of dopant ions in the lattice of host material is in this order $E_{surface} < E_{grain\ boundaries} < E_{grain(bulk)}$. In in this work maximum temperature used for

the synthesis of the sample was 1200 ºC, hence, it is possible that due to lack of sufficient thermal energy require for the diffusion of Gd got limited upto surface and grain boundaries. Ming et al. have confirmed inhomogeneous distribution of rare earth metals (Sm, Gd, Pr and Tb) doped ceria using UV -visible and Raman spectroscopy [263].

Thus, higher intensity of peak corresponding to oxygen vacancies may arise due to inhomogeneous distribution of the dopant (Gd) and reduction of Ce^{4+} to Ce^{3+} mainly present at the surface. It is quite possible at 1200 ºC synthesis temperature lack of oxygen in the perovskite oxides synthesized at higher temperature is a common feature and is observed using various types of synthesis [262]. Moreover, Gd^{3+} is also bigger in size. Hence, the situation demands space and charge compensation by a smaller in size and more charged ion. Hence, an increment in Ce^{3+} concentration is logical.

In this situation oxygen vacancies enrich at the surface of the sample, and hence concentration of surface oxygen vacancies of the sample obviously be higher than that of its internal layer. Therefore, the doping Gd contents may decrease rapidly from the outer surface to the inner layer of samples.

5.4 Conclusion

A few compositions of solid solution $SrCe_{1-x}Gd_xO_3$ (x = 0.0, 0.02, 0.4, 0.6 and 0.10) have been synthesized by solid state reaction method. Rietveld refinement of XRD data has confirmed orthorhombic crystal structure and Pnma space group for all the samples. The crystal structure, lattice strain and crystallite size have been analysed. An increase in lattice parameter may be attributed to substitution of Ce with larger Gd ion. Phase purity and defects have been studied using Raman spectroscopy. Raman measurement shows presence of small amount of impurity phases $SrCO_3$ and CeO_2. Further this technique has indicated presence of oxygen vacancies related defects on Gd substitution. Local structure measurements show that Gd substitution leads to oxygen vacancies which does change host lattice structure notably. Presence of trace

amount of $SrCO_3$ in the synthesized samples has been reconfirmed using FTIR and TGA-DSC measurement. UV-Vis measurement is used for studying the effect of substitution on bandgap and disorder. $Ce^{4+} \rightarrow Ce^{3+}$ conversion increases with Gd substitution. SEM images of sintered samples exhibited decrease in the average grain size on increasing Gd concentration. Precipitation of $SrO/SrCO_3$ at the grain boundaries on increasing Gd concentration is observe, attributed to occupancy of some of Gd ions at Sr sites. Results of complex plane impedance analysis exhibited that composition with x=0.02 has highest value of conductivity (1.24×10^{-3} Scm^{-1}). Lower value of conductivity in higher concentration of Gd is attributed to segregation of SrO at grain boundaries and clustering of oxygen vacancies. X-ray photoemission studies has indicated presence of Ce in mixed valence state (both Ce^{3+} and Ce^{4+} states) and large number of oxygen vacancies at the surface of the sample x=0.02.